Available online at www.sciencedirect.com
ScienceDirect
Applied Surface Science 253 (2007) 5240–5249
applied surface science
www.elsevier.com/locate/apsusc

Synthesis and characterization of single- and co-doped SnO_2 thin films for optoelectronic applications

I. Saadeddin [a], B. Pecquenard [a,*], J.P. Manaud [a], R. Decourt [a], C. Labrugère [a], T. Buffeteau [b], G. Campet [a]

[a] *Institut de Chimie de la Matière Condensée de Bordeaux (CNRS-UPR 9048), Université Bordeaux I, 87 avenue du Dr. Albert Schweitzer, 33608 Pessac cedex, France*

[b] *LPCM, Université Bordeaux I, 351 cours de la libération, 33405 Talence cedex, France*

Received 26 July 2006; received in revised form 24 November 2006; accepted 28 November 2006
Available online 16 January 2007

Abstract

Doped SnO_2 thin films have been prepared by sputtering from two different targets: antimony doped tin oxide (ATO) and antimony and zinc doped tin oxide (AZTO). In the case of ATO ceramic, the antimony amount only reaches 0.012 mol per formula unit due to its evaporation at high temperature while the presence of Zn^{2+} in AZTO prevents the antimony evaporation, greatly enhances the ceramic density and allows the deposition of thin films with a high deposition rate. Both types of thin films have a dense morphology with a smooth surface and they are polycrystalline. For post-annealed ATO thin films, the Drude model was applied to deduce the carrier concentration, the optical mobility as well as the resistivity. The carrier concentration is around ten times higher for ATO thin films compared to AZTO. The two combined effects (higher carrier concentration and mobility) for ATO thin films doped with 1.2% of Sb lead to the best optoelectronic performances, confirming previous results obtained with ceramics. Nevertheless, we have a better opportunity to modulate the conductivity in the case of AZTO thin films.

© 2006 Elsevier B.V. All rights reserved.

Keywords: Antimony and/or zinc-doped tin oxide; Sputtering; Transparent conducting film

1. Introduction

Undoped tin dioxide is a wide bandgap semiconductor ($E_g \sim 3.6$ eV) with electrical resistivity varying from 10 to 10^6 Ω cm, depending on the temperature and the stoichiometry of the oxide [1–4]. In the form of thin films, it is a transparent material, characterized by high optical transmission in the visible range (~90%) [5]. The electrical resistivity was found to drastically decrease by doping with F^- or Sb^{5+} without significant changes in its optical transmittance [6–11]. The corresponding doped materials were, respectively, named FTO and ATO. The properties of FTO and ATO films make them very attractive for various optoelectronic applications (photovoltaic cells, liquid crystal displays, photodetectors, ...) [12–14].

Doped and undoped SnO_2 can be prepared using various techniques, such as sol–gel [15], chemical vapor deposition [16], spray pyrolysis [17,18], pulsed laser deposition [19] and sputtering [20].

A previous study [21] has shown that the co-doping of SnO_2 based ceramics with Sb^{5+} and Zn^{2+}, symbolized as AZTO, noticeably enhances the properties of SnO_2 by combining the advantages of Sb^{5+} which increases the electrical conductivity and Zn^{2+} which greatly improves the ceramic density.

For ceramics, the best result in term of electronic conductivity has been obtained with the following composition $Sn_{0.892}Sb_{0.053}Zn_{0.055}O_{2-\delta}$, determined by electron probe X-ray microanalysis (EPMA). The high electronic conductivity, typically 0.7×10^2 S/cm at 273 K, was attributed to the enhancement of grain percolation, leading to an increase of the carrier mobility [21].

In the present study, we report on the deposition and the characterization of doped SnO_2 thin films obtained by radio frequency magnetron sputtering using two different ceramic

* Corresponding author. Tel.: +33 5 40 00 33 03; fax: +33 5 40 00 66 98.
E-mail address: pecquen@icmcb-bordeaux.cnrs.fr (B. Pecquenard).

0169-4332/$ – see front matter © 2006 Elsevier B.V. All rights reserved.
doi:10.1016/j.apsusc.2006.11.049

Table 1
Ceramic and thin film compositions determined by EPMA and bulk density of targets

Ceramic and thin film identification	Starting mixture	Ceramic final composition	Bulk-ceramic density (g/cm^3)	Thin film composition
ATO	$(SnO_2)_{0.94}$ + $(Sb_2O_3)_{0.03}$	$Sn_{0.988}Sb_{0.012}O_2$	3.79 ± 0.05	$Sn_{0.985}Sb_{0.015}O_2$
AZTO	$[(SnO_2)_{0.94} + (Sb_2O_3)_{0.03}]_{0.94}$ + $(ZnO)_{0.06}$	$Sn_{0.892}Sb_{0.053}Zn_{0.055}O_{2-\delta}$	6.42 ± 0.05	$Sn_{0.888}Sb_{0.060}Zn_{0.052}O_{2-\delta}$

targets having the following compositions, respectively (see Table 1):

- SnO_2 doped with 1.2% of Sb (leading to ATO thin films);
- the previously mentioned composition containing the two doping elements (leading to AZTO thin films).

The aim of this work is to give an insight on how the deposition conditions influence the deposition rate, the composition, the structure, the optical and electrical properties of the produced films. Therefore, a set of complementary investigation methods has been used to characterize the thin films. The chemical compositions have been determined using electron probe X-ray microanalysis (EPMA), X-ray photoelectron spectroscopy (XPS) and Auger electron spectroscopy (AES). Scanning electron microscopy (SEM) and atomic force microscopy (AFM) have been used to study the surface morphology. A structural analysis has been carried out using X-ray diffraction (XRD). The optical characteristics (transmittance and reflectance) have been evaluated in the UV–vis–IR spectral range. In addition, calculations have been carried out in order to determine the carrier densities as well as the optical mobilities by using the Drude model. Finally, the electronic properties have been evaluated by XPS, resistivity and Hall measurements.

2. Experimental

ATO and AZTO thin films were prepared by radio frequency magnetron sputtering in a turbo-pumped sputtering chamber (Leybold L560) using the two above quoted targets (Table 1), both targets having a diameter of 50 mm. The two targets were prepared by cold pressing (200 MPa) and sintered at 1300 °C under air for 12 h. The powders were prepared in the laboratory starting from SnO_2 (99.9%, Aldrich), Sb_2O_3 (>99%, Prolabo) and ZnO (99.9%, Aldrich). Powders were obtained by ball milling for 3 h in an agate bowl containing agate balls and ethanol using a mixture of appropriate amounts of the selected oxides.

Prior to each deposition, vacuum was applied into the chamber until the pressure was about 5–9 × 10^{-5} Pa. All the thin films were deposited at room temperature with no intentional heating of the substrates, and a target to substrate distance equal to 5 cm. A nominal rf power density was varied from 1.5 to 3.5 W/cm^2. Before deposition, a pre-sputtering has been achieved systematically for 20 min in order to clean the target surface. The films were deposited at 1 Pa total gas pressure under a mixture of purified argon (purity > 99.9999%) and oxygen (99.995%) with oxygen partial pressure (P_{O_2}) varying between 0 and 4%. The thin films were deposited on glass substrates for various deposition times. Note that some samples were post-annealed after deposition under vacuum at ~4 × 10^{-4} Pa.

Thin films compositions were determined by EPMA using a CAMECA SX100 spectrometer. The oxidation state for Sb has been determined by XPS using a VG 220i-XL Escalab spectrometer with a monochromatized Al Kα source ($h\nu$ = 1486.6 eV), a 250 μm spot size and a 20 eV pass energy for high-resolution spectra. Energy calibration for XPS was done using silver. Auger electron spectroscopy (AES) was carried out with a VG MICROLAB 310 F in order to analyze the thin film homogeneity over thickness.

The thin film surfaces were observed by field emission scanning electron microscopy (FESEM) using a JEOL JSM-6700F microscope. The surface morphologies were also examined using a VEECO Dimension 3100 atomic force microscope (AFM) under tapping mode. The structural properties of the thin films were studied by X-ray diffraction using a Philips PW1820 diffractometer in Bragg–Brentano geometry using Cu Kα radiation.

Resistivity measurements were carried out as a function of the temperature, from 4.2 K to room temperature using a standard four probe configuration set-up with direct current. The Hall measurements were done using the Physical Properties Measurements System (PPMS) from Quantum Design, by varying the temperature from 4.2 to 300 K and the magnetic field from 0 to 9 T for each specific temperature.

The transmission spectra of the doped tin oxide films in the UV–visible–NIR region have been recorded using a Carry 5000 spectrometer. Reflectance infrared spectra were recorded at a spectral resolution of 8 cm^{-1} using a Fourier transform infrared (FT-IR) spectrometer (Thermo Optek Nexus 670). The reflectance experiments were performed using an external reflection attachment at an angle of incidence of 12°. A computer program has been used to calculate the optical mobility, the carrier concentration and the resistivity parameters from the reflectance infrared spectra.

3. Results and discussion

3.1. Deposition rate

We have studied the influence of three different sputtering parameters on the deposition rate of ATO thin films (Fig. 1). First, the deposition rate increased gradually with the applied radio frequency power density between 1.5 and 3.5 W/cm^2 due to higher plasma density and momentum transfer to the target (Fig. 1a). When the power density was increased from 1.5 to

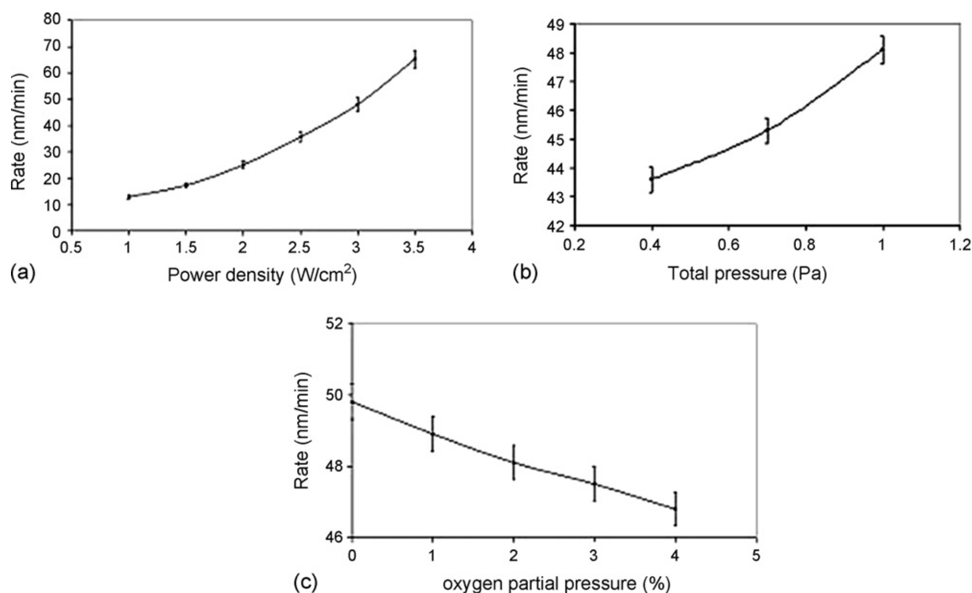

Fig. 1. Deposition rates of ATO thin films according to the sputtering power density (a), the total pressure (b) and the oxygen partial pressure (c). Unless varied within one series of experiments, the parameters were fixed at the following values: P = 3 W/cm^2, P_{total} = 1 Pa and $P_{O_2} = 2\%$.

3.5 W/cm^2, the deposition rate was almost multiplied by 4. An increase of the rate is also observed when the total pressure increases from 0.4 to 1 Pa (Fig. 1b). In fact, it is well known that two opposite phenomena have to be considered when the total pressure is increased:

- First, the number of argon ions that reach the target is higher. Consequently, the number of ejected particles is more important.
- Second, the mean free path of sputtered particles becomes smaller (it is inversely proportional to the total pressure). So, the probability for these particles to sustain collisions will be more important, this induces a decrease of the number of particles that reach the substrate.

In our conditions, the first phenomenon seems to be preponderant. The presence of even small amounts of oxygen in the plasma ($P_{O_2} = 1\%$) has an effect on the deposition rate (Fig. 1c). Indeed, the deposition rate decreases slowly with the initial addition of oxygen to the discharge gas. This phenomenon can be related to the nature of the species present in the plasma (molecular ions present in a mixed plasma that have a lower mean free path inducing a lower probability for particles to reach the substrate) or to the composition of the target surface that varies according to the nature of plasma and can influence the deposition rate.

Similar evolutions have been observed for AZTO thin films. Nevertheless, whatever the sputtering conditions the deposition rate is always higher from about 15 to 25% (depending on the sputtering conditions), for AZTO thin films compared to ATO thin films. This is due to the higher density of the corresponding AZTO target: 6.42 g/cm^3 instead of 3.79 g/cm^3 for ATO target (Table 1). Indeed, this result is in full agreement with literature indicating that target density has a drastic effect on the deposition rate [22] even if it is always suitable to have a dense target.

3.2. *Chemical composition and oxidation states*

The compositions of the ATO and AZTO ceramic targets and of the corresponding thin films deposited under a power density of 3 W/cm^2, a total pressure of 1 Pa, an oxygen partial pressure equal to 2% and a target-to-substrate distance of 5 cm (note that these sputtering parameters lead to the best compromise between a high transparency and a high conductivity as will be seen later) are shown in Table 1. As we have seen previously [21], in the case of ATO ceramic, the antimony content reaches only 0.012 mol per formula unit whereas in the AZTO system, the solid solubility of Sb is higher (Table 1). The main origin of this solubility difference may be attributed to the likely isovalent substitution of two Sb^{5+} and one Zn^{2+} for three Sn^{4+}, thereby maintaining charge neutrality as well as structural integrity. In addition, the ceramic shrinkage due to Zn doping may also prevent antimony departure in AZTO (note that the bulk density is greatly enhanced in this case, as noticed in Table 1). There is a good accordance between the compositions of ceramics and thin films, only a slightly higher amount of antimony is observed into thin films (Table 1). Note that thin films compositions for as-deposited and annealed films are quite equivalent. AES analyses have also shown that the chemical composition is quite homogeneous in the targets and over the whole thin film layer thickness.

In order to investigate the formal oxidation state for antimony ions (all tin ions being present as Sn^{4+}), XPS measurements were carried out on ceramic targets and on ATO and AZTO thin films. As a preliminary step, several reference compounds have been characterized: Sb_2O_5, Sb_2O_4 and Sb_2O_3. The binding energies for the different reference compounds and all data for ceramics and thin films are reported on Table 2. Note that for reference compounds, the shift in energy between Sb^{3+} and Sb^{5+} is only 0.5 eV. The XPS spectra of the Sb4d core peaks for ceramic targets and corresponding thin films are,

Table 2
XPS Sb^{5+}, Sb^{4+} and Sb^{3+} $4d_{5/2–3/2}$ binding energies (eV) as well as the full width at half maximum (in parentheses) for reference compounds, ceramics used for the targets and the thin films of ATO (as-deposited and annealed at 500 °C under vacuum)

	Sb^{5+} $4d_{5/2–3/2}$ (eV)	Sb^{4+} $4d_{5/2–3/2}$ (eV)	Sb^{3+} $4d_{5/2–3/2}$ (eV)
References			
Sb_2O_5	35.0–36.2 (2.20), 100%		
Sb_2O_4		34.7–35.9 (1.96), 100%	
Sb_2O_3			34.5–35.7 (1.57), 100%
Ceramics for target			
ATO	34.9–36.2 (1.35), 69%		34.3–35.6 (1.25), 31%
AZTO	35.0–36.2 (1.35), 100%		
Thin films			
As-deposited AZTO	35.0–36.2 (1.10), 29%		34.4–35.6 (1.10), 71%
Annealed AZTO	34.9–36.1 (1.10), 44%		34.3–35.5 (1.10), 56%

respectively, shown in Figs. 2 and 3. We have selected the Sb4d peak because the Sb3d is overlapped with a peak of Sn3d.

Considering the XPS measurements for ceramic targets (Fig. 2), two different results have been obtained:

(i) For ATO target (Fig. 2a), the presence of both Sb^{5+} and Sb^{3+} are detected with a deduced ratio Sb^{3+}/Sb^{5+} equal to ~30/70. This implies that ~0.008 out of 0.012 Sb exists as Sb^{5+} in the ceramic final composition (Table 1), the rest of antimony being in the Sb^{3+} state (~0.004). From the carrier concentration calculated from Hall measurements (1.2×10^{20} cm^{-3} [21]), one can deduce that the Sb^{5+} content responsible for the electronic conductivity is equal to 0.004, according to the normally expected formula represented by:

$$Sn^{4+}_{0.996}Sb^{5+}_{0.004}O_2[0.004e^-]. \quad \text{(a)}$$

However, this value is two times lower than the above reported one (0.008). The difference (~0.004) should correspond to the number of Sb^{5+} which have been 'compensated' by an equal number (i.e. ~0.004) of Sb^{3+}, thereby maintaining charge neutrality without creation of additional electron carriers. In other words, Sb^{3+} would reduce the carrier concentration generated by Sb^{5+}. Consequently, formula (a) should be more accurately expressed as:

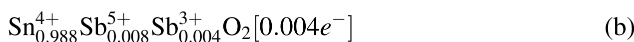

$$Sn^{4+}_{0.988}Sb^{5+}_{0.008}Sb^{3+}_{0.004}O_2[0.004e^-] \quad \text{(b)}$$

(ii) For AZTO target (Fig. 2b), only one component with a pronounced maximum around 35.0 eV is observed, corresponding to Sb^{5+}. For AZTO, the carrier concentration is equal to 1×10^{20} cm^{-3} [21]. The deduced number of electrons per formula unit is ~0.004. This value is far from the Sb molar ratio measured by EPMA which is equal to 0.053 (see Table 1). This discrepancy would imply that part of Zn^{2+} reduces the carrier concentration produced by Sb^{5+} according to:

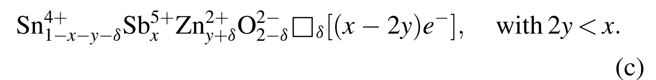

$$Sn^{4+}_{1-x-y-\delta}Sb^{5+}_{x}Zn^{2+}_{y+\delta}O^{2-}_{2-\delta}\square_{\delta}[(x-2y)e^-], \quad \text{with } 2y < x. \quad \text{(c)}$$

Hence, $x - 2y \sim 0.004$. As x is equal to 0.053, one gets $y \sim 0.024$. On the other hand, the molar ratio of Zn^{2+} reported in Table 1 is ~0.055. Therefore, according to the formula, we can calculate δ which represents the molar ratio of neutral oxygen vacancies: $\delta = 0.055 - 0.024 = 0.031$.

In the case of thin films, no reliable results have been obtained by XPS for ATO films. Indeed, the too low amount of antimony (1.5% as indicated in Table 1) corresponds to the limit of XPS-signal detection. However, one can reasonably assume that Sb^{5+} and Sb^{3+} coexist in ATO films, as it occurred for ATO ceramics. For AZTO thin films, the Sb4d core peak present two components (Fig. 3): the most important, located at lower binding energies corresponds to Sb^{3+} while the other located on the higher energy side is attributed to Sb^{5+}.

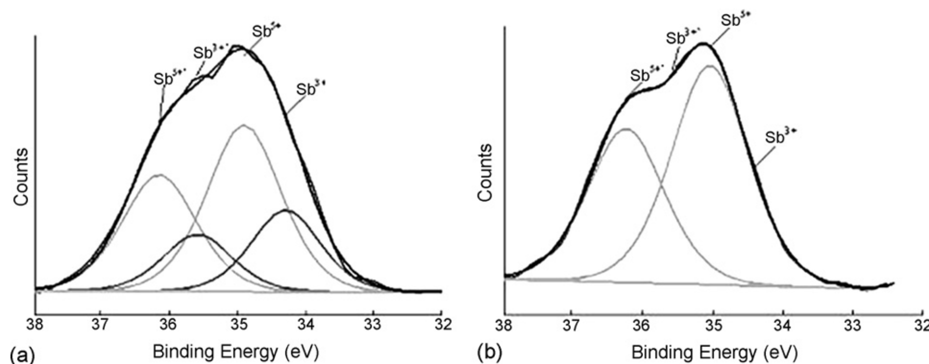

Fig. 2. XPS Sb4d core peaks for ATO (a) and AZTO (b) ceramics used to prepare the targets.

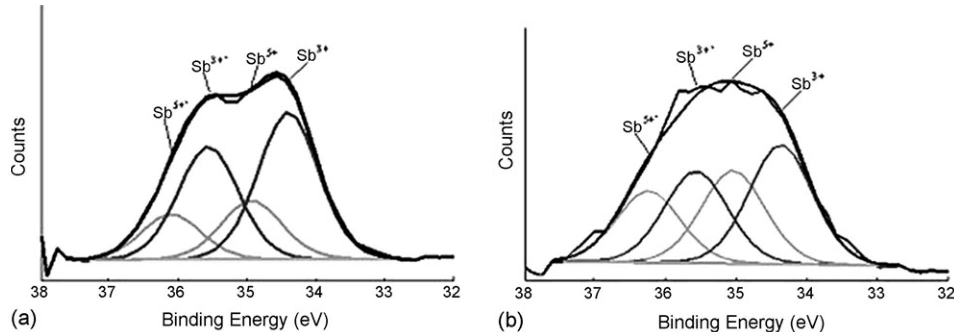

Fig. 3. XPS Sb4d core peaks for as-deposited AZTO (a) and annealed at 500 °C under vacuum (b) thin films.

The difference in Sb formal state between the target and the film can be explained by a slight reduction of the AZTO target surface under the argon ions bombardment during sputtering. As the thin films are deposited under a low oxygen partial pressure, the reduced antimony species cannot be re-oxidized in the sputtering chamber. Taking into account the above XPS results for AZTO thin film, we can expect that Sn^{4+} is also partially substituted by the other species present in the thin film, i.e. Zn^{2+} and Sb^{3+} that would reduce the carrier concentration produced by Sb^{5+} according to:

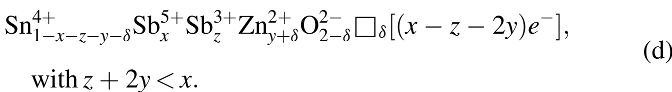

$$Sn^{4+}_{1-x-z-y-\delta}Sb^{5+}_{x}Sb^{3+}_{z}Zn^{2+}_{y+\delta}O^{2-}_{2-\delta}\square_{\delta}[(x-z-2y)e^{-}],\quad \text{with } z+2y<x. \qquad (d)$$

Nevertheless, we have an extra amount of Sb^{3+} and Zn^{2+}, which are probably segregated at the grain boundaries forming planar defects and/or other phases.

Post-annealed films show an enhancement of the Sb^{5+} amount from 29 to 44% (see Table 2 and Fig. 3), meaning that a part of Sb^{3+} is oxidized during annealing. Since annealing occurs under vacuum, one may assume that the Sb^{3+} species have been oxidized by chemisorbed OH^{-} species present on the film surface. This is confirmed by Infrared transmittance spectra for ATO thin films (Fig. 4). The hydroxyl group bands at ~2800 nm are drastically decreased after annealing the films. These results are in agreement with the results obtained by Geraldoa et al. [23] for ATO films deposited via sol–gel. The OH^{-} species, which are strongly attached to the film surface, usually begins to be desorbed, at ~250 °C [23,24], while oxidizing Sb^{3+} into $Sb^{5+}$and generating electron carrier in the

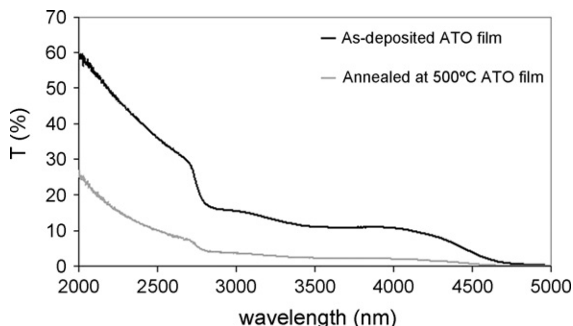

Fig. 4. Infrared transmittance spectra for as-deposited ATO thin films and annealed at 500 °C.

conduction band. This process could be depicted as:

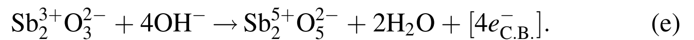

$$Sb^{3+}_{2}O^{2-}_{3} + 4OH^{-} \rightarrow Sb^{5+}_{2}O^{2-}_{5} + 2H_2O + [4e^{-}_{C.B.}]. \qquad (e)$$

According to (e), an increase of the electron-carrier density should occur during the annealing process of AZTO films, concomitant with the oxidation of the Sb^{3+} species. This point will be discussed afterwards.

3.3. Structure and morphology of thin films

Whatever the target used, the thin film is dense with a smooth surface (Fig. 5). From AFM, it can be seen that by increasing the annealing temperature, the roughness is increased (Fig. 6). Indeed, the Ra, which is the arithmetic average deviation from the mean line within the assessment length, also increases from 0.45 nm (as-deposited) to 0.50 nm (annealed at 500 °C) for ATO and from 0.69 nm (as-deposited) to 0.86 nm (annealed at 500 °C) for AZTO thin films.

Figs. 7 and 8, respectively, show the X-ray diffraction spectra for ATO and AZTO films deposited on glass substrates. The (1 1 0), (1 0 1), (2 1 1) and (3 0 1) diffraction peaks (ICDD card number 41–1445) are mainly observed. The films are polycrystalline and retained the rutile structure. As expected, for ATO thin film, there is no evidence of the presence of extra phases such as antimony oxides (Sb_2O_3 or Sb_2O_5) suggesting the formation of a solid solution. Moreover, the molar ratio of Sb may be too low to be detected. However, some authors have proposed that a part of Sn^{4+} ions in the SnO_2 lattice are replaced not only by Sb^{5+} ions, but also by Sb^{3+} ions [25], this is also in agreement with formula (b). Moreover, the substitution of Sn^{4+} by Sb^{3+} accounts for the slight shift of the main diffraction peaks towards lower angles compared to pure SnO_2, which induces an increase of the cell parameters (Figs. 7 and 8). Indeed, the ionic radius for the six-coordinated Sn^{4+} (0.83 Å) is smaller than that of Sb^{3+} (0.90 Å) [26]. However, one must also consider that Sb^{3+} behaves as a non-ionized donor center having its $5s^2$ electron stabilized below the conduction band edge. It means that Sb^{3+} should have a somewhat different structural environment than Sb^{5+} species which behave as ionized donor centers (according to formula (a)). Hence, Sb^{3+} were assumed by Messad et al. [18] to segregate at the grain surfaces and also at grain boundaries forming planar defects.

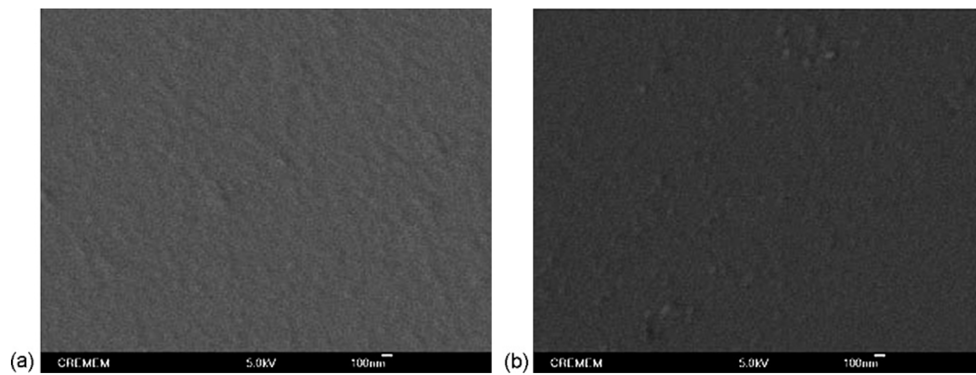

Fig. 5. SEM micrographs of ATO thin films as-deposited (a) and annealed at 500 °C under vacuum (b). The sputtering conditions are the following: $P = 3$ W/cm^2, $P_{total} = 1$ Pa and $P_{O_2} = 2\%$.

The intensity of the (2 1 1) peak increases with the annealing temperature, showing the existence of a preferential orientation (note that this preferential orientation is strongly influenced by the oxygen partial pressure). The crystallite sizes for the samples have been determined by a well-known Scherrer formula [27] from diffraction lines 1 1 0 (the broadest one) and 2 1 1 (the narrowest one). For both orientations, we observe an increase of the crystallite size with the annealing temperature from 7 to 9 nm for (1 1 0) and from 26 to 31 nm for (2 1 1).

In the case of AZTO thin films, the SnO_2 peaks intensity ratios are closer to thus observed for the relative powder and they are broader than those observed for ATO thin films accounting for a smaller crystallite size. In addition, the slight shift of the peaks towards lower angle confirms the existence of Sb^{3+} in substitutional position (formula (d)).

3.4. Optical properties

We have first studied the influence of the oxygen partial pressure, the annealing temperature and the thickness of the ATO thin films deposited on glass substrate on the transparency and/or the reflectivity. The oxygen partial pressure has a strong influence on the transmission in the visible part. For $P_{O_2} = 1\%$, the best transmission reaches 80% whereas it goes up to 90%

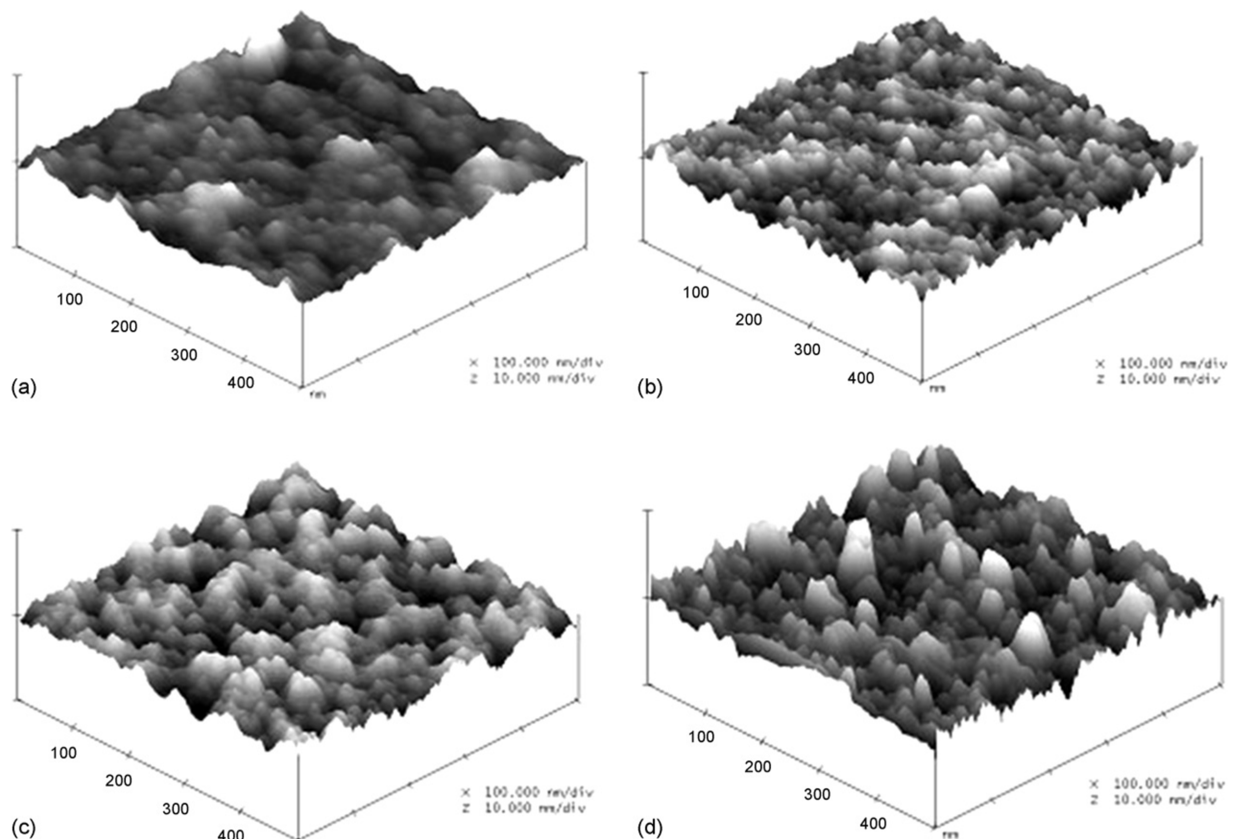

Fig. 6. AFM figures obtained in the tapping mode for as-deposited ATO (a) and annealed at 500 °C under vacuum (b) thin films and as-deposited AZTO (c) and annealed at 500 °C under vacuum (d) thin films.

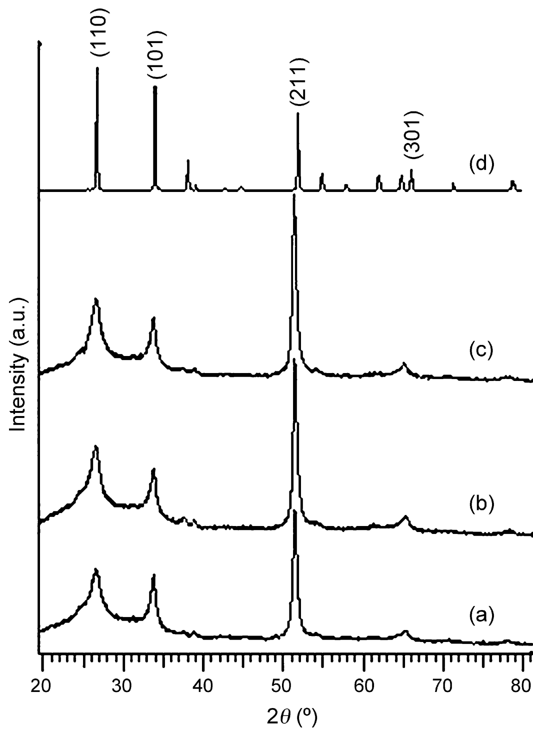

Fig. 7. X-ray diffraction patterns of ATO thin films as-deposited (a), annealed at 250 °C (b) and 500 °C under vacuum (c). The pattern of SnO_2 powder is given for comparison (d).

for an oxygen partial pressure equal to 4% (Fig. 9a). Indeed, at low oxygen partial pressure, the films have brown color and are nearly colorless for $P_{O_2} = 4\%$ (with only a slight difference

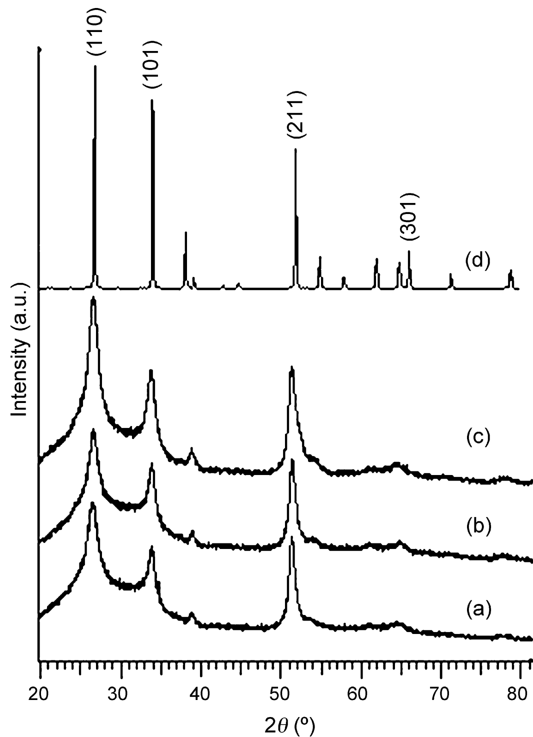

Fig. 8. X-ray diffraction patterns of AZTO thin films as-deposited (a), annealed at 250 °C (b) and 500 °C under vacuum (c). The pattern of SnO_2 powder is given for comparison (d).

between 2 and 4%). In the case of annealed thin films, the best transparency is obtained for $P_{O_2} = 2\%$. For this peculiar value, we notice almost similar optical results for as-deposited and annealing thin films in the visible part (Fig. 9b). In the IR spectral range, the transparency decreases and the reflectivity increases as annealing temperature increases (reflectivity increases up to 35% for films annealed at 250 °C and 60% for films annealed at 500 °C). Note that the properties of the thin films annealed at 250 °C are close to those obtained for the as-deposited one. A similar behavior is observed when the thickness is increased from 520 to 960 nm (Fig. 9c). In addition, as expected a slight decrease of the transparency is also noticed in the visible part for thicker film. Note that all previous experiments have been done on thin films having a thickness equal to 520 nm (standard condition).

By using the Drude model, we have fitted the reflectance infrared spectra in order to determine the values of important parameters such as the optical mobility and the carrier concentration. Indeed, accordingly to Drude's theory, for free electrons in metals, the real and imaginary parts of the dielectric function, respectively, symbolized by ε_1 and ε_2 can be expressed as:

$$\varepsilon_1 = n^2 - k^2 = \varepsilon_\infty \left(1 - \frac{\omega_P^2}{\omega^2 + \gamma^2}\right) \quad (1)$$

$$\varepsilon_2 = 2nk = \varepsilon_\infty \frac{\omega_P^2 \gamma}{\omega(\omega^2 + \gamma^2)} \quad (2)$$

where n, k and ε_∞ denotes, respectively, the real, the imaginary part of the refractive index and the high frequency dielectric constant of the thin film. ω_P represents the plasma resonance frequency given by:

$$\omega_P = \frac{2\pi c}{\lambda_P} = \left(\frac{Ne^2}{\varepsilon_0 \varepsilon_\infty m_e^*}\right)^{1/2} \quad (3)$$

where N represents the charge carrier concentration, m_e^* the electron effective mass, e the electronic charge, and c is the speed of light in vacuum. The charge carrier damping constant γ equal to $1/\tau$ (where τ is the relaxation time) is related to the optical mobility μ by the relation:

$$\gamma = \frac{1}{\tau} = \frac{e}{m_e^* \mu}. \quad (4)$$

When the thickness of the layer is greater than the skin depth $\delta(\lambda/4\pi k)$, the reflectance is given by:

$$R = \frac{(n-1)^2 + k^2}{(n+1)^2 + k^2} \quad (5)$$

From Eqs. (1)–(4), one can calculate n and k values from the plasma resonance frequency ω_P, the carrier concentration (N, in cm^{-3}) and the optical mobility (μ, in $cm^2/(V\ s)$). Then, the minimization of the difference between the theoretical reflectance spectrum calculated from Eq. (5) and the experimental reflectance spectrum allows the fit of the above quoted optical parameters. The values of carrier concentration

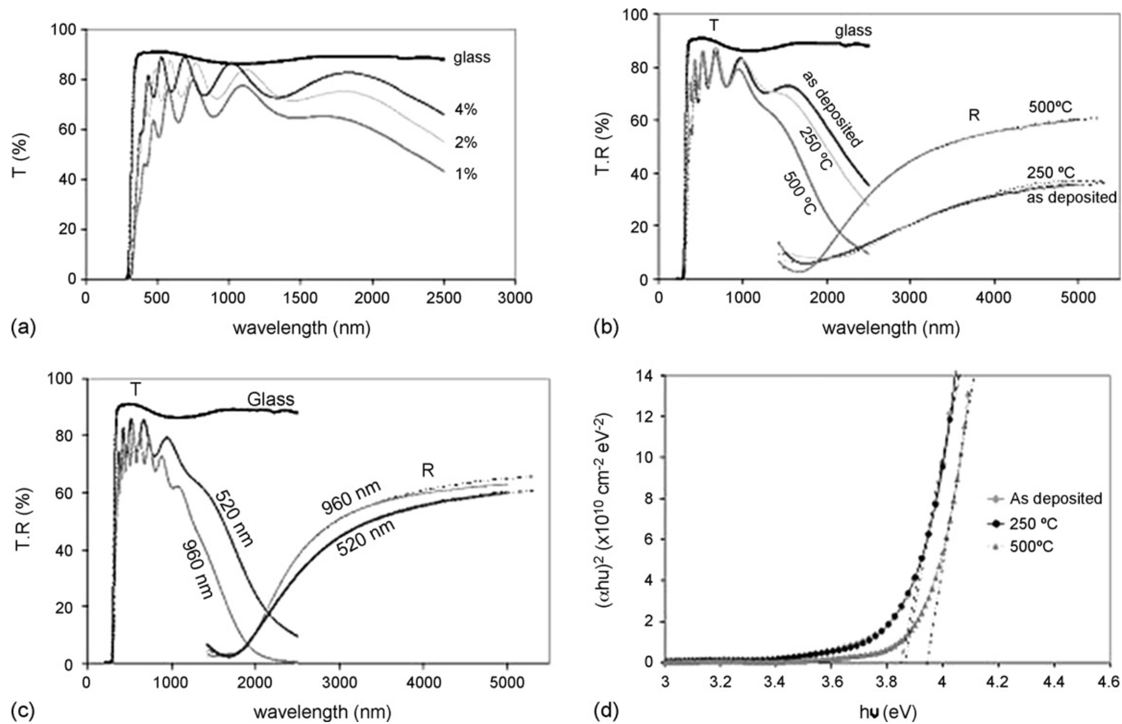

Fig. 9. Optical properties of ATO thin films. (a) Transmittance spectra as a function of oxygen partial pressure. (b) Transmittance and reflectance spectra as a function of annealing temperature. (c) Transmittance and reflectance spectra of the films with different thickness. (d) Calculation of optical band gap. *Note*: Dashed reflectance spectra lines represent the calculated values (Drude model).

and mobility thus deduced, by assuming a carrier effective mass of $0.25m_e$, have been compared with those deduced from Hall and conductivity measurements (Table 3). There is a good agreement between calculation and experiment except for as-deposited ATO film. Indeed, for this compound, the slight decrease of the resistivity when the temperature increases (as shown later in Fig. 12), indicates that it corresponds to the limit of the Drude model validity.

We have also determined the direct optical band gap for different thin films (as-deposited or annealed). The fundamental absorption which corresponds to electron excitation from the valence band to the conduction band can be used to determine the value of the optical band gap. For all studied samples, the $\alpha(h\nu)$ curves correspond to the case of a crystalline material with direct allowed transitions (direct gap) according to the following equation:

$$\alpha(\mathrm{h}\nu) = A^*(h\nu - E_g)^{1/2} \qquad (6)$$

where α is the absorption coefficient and A^* is a constant depending on the material and the direct optical bandgap (E_g). From the plot, E_g is determined by extrapolating the linear portion of the plotted curves (Fig. 9d) to zero absorption. The optical gap is found to vary between 3.85 and 3.95 eV. This variation can be explained by the Burstein–Moss effect [28,29]. It shows that E_g, for the transparent thin film, increases with the carrier concentration. There is a good accordance with literature where the values are varying between 3.9 and 4.5 eV depending on the dopants and preparation method [30–33].

Table 3
Values of mobility, carrier concentration, resistivity and direct gap (E_g) for different ATO and AZTO thin films

	Mobility (cm^2/(V s))		Carrier conc. (cm^{-3})		E_g (eV)	Resistivity (Ω cm)	
	Deduced from calc.	Deduced from Hall	Deduced from calc.	Deduced from Hall		Deduced from calc.	Measured
ATO thin films							
As-deposited	5.7	2.5	2.2×10^{20}	6.76×10^{19}	4.11	4.9×10^{-3}	3.6×10^{-2}
Annealed at 250 °C	6.2	5.7	2.1×10^{20}	1.83×10^{20}	4.12	4.7×10^{-3}	6.0×10^{-3}
Annealed at 500 °C	11.5	11.1	2.7×10^{20}	2.65×10^{20}	4.17	2.0×10^{-3}	2.1×10^{-3}
AZTO thin films							
As-deposited	–	2.3	–	1.62×10^{18}	4.02	–	1.50
Annealed at 250 °C	–	1.8	–	1.26×10^{19}	4.04	–	0.27
Annealed at 500 °C	–	0.9	–	3.68×10^{19}	4.07	–	0.17

In the case of ATO thin films, the Drude model was applicable and some values were deduced from the fit of the reflectivity curves. Note that for calculated values deduced from optical measurements, m^* the effective mass is considered to be equal to $0.25m_e$.

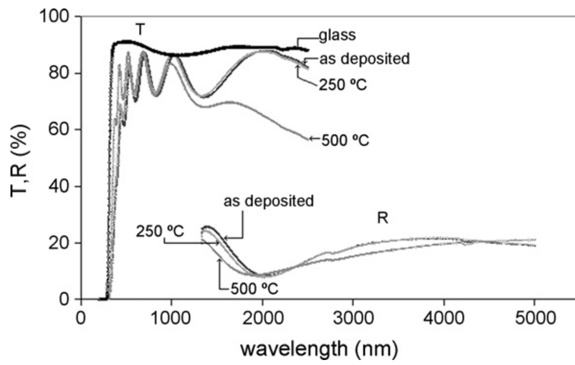

Fig. 10. Transmittance and reflectance spectra for AZTO thin films—influence of the post-annealing temperature.

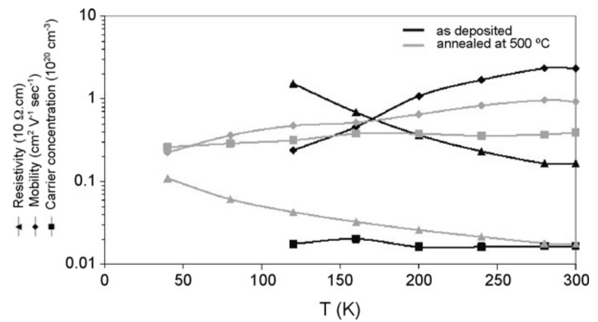

Fig. 12. Evolution of resistivity, Hall mobility and carrier concentration as a function of temperature for as-deposited and annealed at 500 °C under vacuum AZTO thin films.

If we take into account all the optical results obtained for ATO thin films, we can conclude that the best performances have been reached with films having a 520 nm thickness, annealed at 500 °C under vacuum and prepared under $P_{O_2} = 2\%$, a 1 Pa total pressure and a power density of 3 W/cm^2 (giving a good compromise between a high deposition rate and an enhanced life time of the target).

If we consider ATZO thin films, the transparency in the visible spectral range is similar to the one obtained for ATO thin films prepared in similar optimum conditions (Fig. 10). However, a very weak reflectivity is obtained whatever the annealing temperature. As these AZTO do not have a metallic behavior (rather a semiconductor behavior), the Drude model was not applicable to fit the reflectivity curves. The direct gap is slightly lower ($E_g \approx 3.6$ eV for as-deposited) than for ATO thin films indicating that the carrier concentration is also lower (Table 3), according to Burstein–Moss effect [29,30].

3.5. Electrical properties

First, we have followed the evolution of the resistivity as a function of the oxygen partial pressure for ATO annealed thin films. The lowest value of resistivity ($3 \times 10^{-2}\ \Omega$ cm) is obtained for an oxygen partial pressure equal to 2%, in good accordance with the results of transmittance. For lower or higher oxygen partial pressure, the values of resistivity are comprised between ($9.5 \times 10^{-2}\ \Omega$ cm) and ($4.7 \times 10^{-1}\ \Omega$ cm). Then we have studied the electrical performances of thin films prepared under the optimum conditions summarized at the end of Section 3.4.

Figs. 11 and 12 give the temperature influence upon the carrier concentration, the Hall mobility and the resistivity for ATO and AZTO thin films as-deposited and annealed at 500 °C under vacuum. All the results obtained at room temperature are summarized in Table 3. For all samples, the negative sign of the Hall coefficient accounts for the n-type conductivity of the thin films.

For ATO thin films, whatever the measurement temperature, we have clearly noticed an increase of the mobility and the carrier concentration with the annealing temperature. Usually when the carrier concentration increases, the mobility decreases. So, the inverse behavior observed in this case is a consequence of an evolution of the structure with the temperature as observed by X-ray diffraction (we observe a significant increase of the crystallites size and thus the crystallinity with the temperature). Indeed, by increasing the size of the crystallite upon annealing, we decrease the density of structural defects (such as distorted coordination polyhedra at the grain surface) thus lowering the number of scattering centers which decrease the carrier life time and therefore the mobility. The simultaneous increase of carrier concentration and mobility leads to a significant decrease of the resistivity from $3.6 \times 10^{-2}\ \Omega$ cm (observed for as-deposited film) to $2.1 \times 10^{-3}\ \Omega$ cm (for 500 °C post-annealed sample), corresponding to values of sheet resistances, respectively, equal to 691 and 38 Ω/□. Excepted for the as-deposited thin film a good

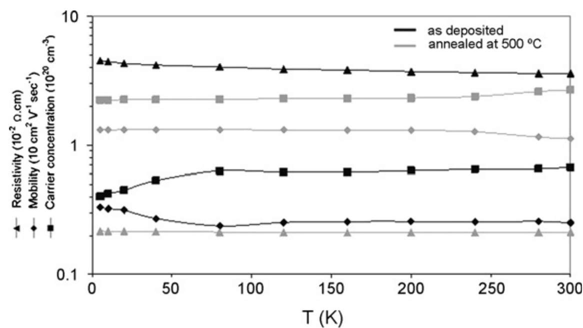

Fig. 11. Evolution of resistivity, Hall mobility and carrier concentration as a function of temperature for as-deposited and annealed at 500 °C under vacuum ATO thin films.

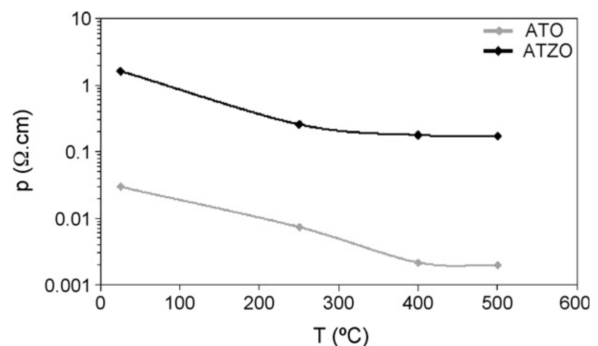

Fig. 13. Comparison of resistivity with post-annealing temperature for ATO and AZTO thin films.

agreement exists between calculated and experimental data (see explanation in Section 3.4).

Concerning AZTO thin films, the crystallite size is lower than for ATO thin films, accounting for a higher density of structural defects at the grain surface and therefore responsible for a lower mobility (Table 3). Moreover, as expected the carrier concentration increases while the mobility decreases when the post-annealing temperature is increased. This results in a decrease of the resistivity. Nevertheless, if we compare the performances of ATO and AZTO thin films, the low values of mobility combined with a carrier concentration, one order of magnitude lower, induces higher value of resistivity for AZTO thin films compared to ATO ones (Fig. 13 and Table 3). This lower value of carrier concentration for AZTO is attributed to Zn^{2+} and Sb^{3+} species in cationic substitutional position, which reduce the carrier concentration, as discussed previously.

4. Conclusion

We have prepared by sputtering two types of doped SnO_2 thin films from two different ceramic targets: antimony doped tin oxide (ATO) and antimony and zinc doped tin oxide (ATZO). A good accordance in composition is observed between ATO and AZTO ceramics and their corresponding ATO and AZTO thin films. The morphology of the films is dense with a smooth surface and they are polycrystalline. We have just observed a slight shift of the main peaks towards lower angles compared to pure SnO_2, which was attributed to the replacement of some Sn^{4+} by Sb^{3+} in the rutile structure. In term of optoelectronic properties, the optimum deposition conditions in order to have high transparency in the visible range and lowest resistivity are the following: $P = 3$ W/cm^2, $P_t = 1$ Pa and $P_{O_2} = 2\%$, for both thin films. The deposition rate for AZTO films was always higher (15–25% depending on the sputtering conditions) due to the higher density of AZTO ceramic target induced by presence of Zn^{2+}. AZTO films have lower carrier concentration than ATO counterparts. Indeed, in the AZTO films, the number of carriers created by Sb^{5+} doping decreases due to the presence of Sb^{3+} and Zn^{2+} in substitutional positions according to $Sn^{4+}_{1-x-z-y-\delta}Sb^{5+}_{x}Sb^{3+}_{z}Zn^{2+}_{y+\delta}O^{2-}_{2-\delta}\square_{\delta}$ $[(x-z-2y)e^{-}]$. The optical band gap decreases from ~3.85 eV for ATO to ~3.61 eV for AZTO due to the Burstein–Moss effect. For ATO films, post-annealing increases both the carrier concentration and the mobility; metal-type conductivity is observed. Hence, Drude model was applied in order to deduce the carrier concentration, the optical mobility as well as resistivity. A good accordance between optical and electrical data was observed. In the case of AZTO films, post-annealing increases the carrier concentration; but the mobility is reduced. Moreover, they show a semiconducting behavior. Thus, the Drude model cannot be applied for AZTO films.

Acknowledgement

The authors thank Michel Lahaye (CECAMA) for Auger and EPMA measurements.

References

[1] E.E. Kohnke, J. Phys. Chem. Solids 23 (1962) 1557.
[2] C.G. Fonstad, R.H. Rediker, J. Appl. Phys. 42 (1971) 2911.
[3] M. Nagasawa, S. Shionya, J. Phys. Soc. Jpn. 30 (1971) 1213.
[4] Z.M. Jarzebski, J.P. Marton, J. Electrochem. Soc. 123 (1976) 299.
[5] E. Dien, J.M. Laurent, A. Smith, J. Eur. Ceram. Soc. 19 (1999) 787.
[6] L.D. Loch, J. Electrochem. Soc. 110 (1963) 1081.
[7] H.E. Matthews, E.E. Kohnke, J. Phys. Chem. Solids 29 (1968) 653.
[8] C.A. Vincent, D.G. Weston, J. Electrochem. Soc. 119 (1972) 518.
[9] P.G. Orsini, P. Pernice, L. Egiziano, J. Electrochem. Soc. 128 (1981) 1451.
[10] P.H. Duvineaud, D. Reinhard, Sci. Ceram. 12 (1984) 287.
[11] U. zum Felde, M. Haase, H. Weller, J. Phys. Chem. B 104 (2000) 9388.
[12] C. Terrier, J.P. Chatelon, J.A. Roger, Thin Solid Films 295 (1997) 95.
[13] G. Sanon, R. Rup, E.A. Mansingh, Phys. Rev. B 44 (1991) 5672.
[14] C. Geoffroy, G. Campet, F. Merril, J. Portier, J. Salardenne, G. Couturier, Active Passive Elec. Comp. 14 (1991) 111.
[15] F. Morazzoni, C. Canevali, N. Chiodini, C. Mari, R. Ruffo, R. Scotti, L. Armelao, E. Tondello, L. Depero, E. Bontempi, Mater. Sci. Eng. C 15 (2001) 167.
[16] K.S. Kim, S.Y. Yoon, W.J. Lee, K.H. Kim, Surf. Coat. Technol. 138 (2001) 229.
[17] J. Zhang, K. Colbow, J. Appl. Phys. 71 (1992) 2238.
[18] A. Messad, J. Bruneaux, H. Cachet, M. Froment, J. Mater. Sci. 29 (1994) 5095.
[19] H. Kima, A. Pique, Appl. Phys. Lett. 84 (2004) 218.
[20] T. Minami, J. Vac. Sci. Technol. A 17 (1999) 1765.
[21] I. Saadeddin, H.S. Hilal, B. Pecquenard, J. Marcus, A. Mansouri, C. Labrugere, M.A. Subramanian, G. Campet, Solid State Sci. 8 (2006) 7.
[22] Y. Hamon, A. Douard, F. Sabary, C. Marcel, P. Vinatier, B. Pecquenard, A. Levasseur, Solid State Ionics 177 (2006) 257.
[23] V. Geraldoa, L.V. de Andrade Scalvib, E.A. de Moraisa, C.V. Santillic, S.H. Pulcinellic, Mater. Res. 6 (2003) 451.
[24] S.D. Han, S.Y. Huang, G. Campet, M.A. Kennard, Y.M. Son, Active Passive Elec. Comp. 18 (1995) 53.
[25] H. Miao, C. Ding, H. Luo, Microelectron. Eng. 66 (2003) 142.
[26] R.D. Shannon, Acta Cryst. A 32 (1976) 751.
[27] P. Scherrer, Gottin Nachr. 2 (1918) 98.
[28] E. Burstein, Phys. Rev. 93 (1954) 632.
[29] T.S. Moss, Proc. Phys. Soc. Lond. Sect. B 67 (1954) 775.
[30] B. Stjerna, E. Olsson, C.G. Granqvist, J. Appl. Phys. 76 (1994) 3797.
[31] E. Shanthi, A. Banerjee, V. Dutta, K.L. Chopra, J. Appl. Phys. 53 (1982) 1615.
[32] E. Shanthi, V. Dutta, A. Banerjee, K.L. Chopra, J. Appl. Phys. 51 (1980) 6243.
[33] A. De, S. Ray, J. Phys. D: Appl. Phys. 24 (1991) 719.